

Discovery of spin-phase-dependent QPOs in the supercritical accretion regime from the X-ray pulsar RX J0440.9+4431

Christian Malacaria¹, Daniela Huppenkothen^{2,3}, Oliver J. Roberts⁴, Lorenzo Ducci⁵, Enrico Bozzo⁶, Peter Jenke⁷, Colleen A. Wilson-Hodge⁸, and Maurizio Falanga¹

¹ International Space Science Institute, Hallerstrasse 6, 3012 Bern, Switzerland
e-mail: cmalacaria.astro@gmail.com

² SRON Netherlands Institute for Space Research, Niels Bohrlaan 4, 2333CA Leiden, The Netherlands

³ Anton Pannekoek Institute for Astronomy, University of Amsterdam, Science Park 904, 1098 XH, Amsterdam, The Netherlands

⁴ Science and Technology Institute, Universities Space and Research Association, 320 Sparkman Drive, Huntsville, AL 35805, USA

⁵ Institut für Astronomie und Astrophysik, Kepler Center for Astro and Particle Physics, Universität Tübingen, Sand 1, 72076 Tübingen, Germany

⁶ Department of Astronomy, University of Geneva, Chemin d'Ecogia 16, CH-1290 Versoix, Switzerland

⁷ University of Alabama in Huntsville (UAH), Center for Space Plasma and Aeronomic Research (CSPAR), 301 Sparkman Drive, Huntsville, Alabama 35899

⁸ ST 12 Astrophysics Branch, NASA Marshall Space Flight Center, Huntsville, AL 35812, USA

November 15, 2023

ABSTRACT

RX J0440.9+4431 is an accreting X-ray pulsar (XRP) that remained relatively unexplored until recently, when major X-ray outburst activity enabled more in-depth studies. Here, we report on the discovery of ~ 0.2 Hz quasi-periodic oscillations (QPOs) from this source observed with *Fermi*-GBM. The appearance of QPOs in RX J0440.9+4431 is triple transient, that is, QPOs appear only above a certain luminosity, only at certain pulse phases (namely corresponding to the peak of its sine-like pulse profile), and only for a few oscillations at time. We argue that this newly discovered phenomenon (with the appearance of triple transient QPOs – or ATTO) occurs if QPOs are fed through an accretion disk whose inner region viscosity is unstable when exposed to mass accretion rate and temperature variations. Such variations are triggered when the source switches to the supercritical accretion regime and the emission pattern changes. We also argue that the emission region configuration is likely responsible for the observed QPOs spin-phase dependence.

Key words. magnetic fields – pulsars: individual: RX J0440.9+4431 – stars: neutron – X-rays: binaries

1. Introduction

The source RX J0440.9+4431 (RX J0440 hereafter) is an accreting X-ray pulsar (XRP) first discovered with *ROSAT* (Motch et al. 1997), and showing X-ray pulsations approximately every 202 s (Reig & Roche 1999). The system is a Be/X-ray Binary with a B0 optical companion, LS V +44 17 (Reig et al. 2005). The source Gaia distance is 2.4 ± 0.1 kpc in DR3 (Gaia Collaboration et al. 2022).

After more than ten years of quiescence, RX J0440 exhibited a major outburst starting on December 2022 and lasting until April 2023 (Nakajima et al. 2022; Mandal et al. 2023; Coley et al. 2023; Pal et al. 2023). Several observations have been dedicated to this bright event. Multiple pieces of evidence show that during the latest outburst the source transitioned from the subcritical to the supercritical accretion regime (Salganik et al. 2023; Doroshenko et al. 2023). These two regimes are characterized by deceleration of the accretion flow dominated at the neutron star (NS) surface by Coulomb interactions and above the NS surface by a radiative shock, respectively, and are separated by the so-called critical luminosity, L_c , on the order of 10^{37} erg/s

(Basko & Sunyaev 1976; Becker et al. 2012; Mushtukov et al. 2015).

The source spectrum can be described with two Comptonized components both at low and high luminosity (Tsygankov et al. 2012; Salganik et al. 2023). A double-hump spectrum was, up to now, observed (see, e.g., Tsygankov et al. 2019, and references therein) and theoretically motivated (Mushtukov et al. 2021; Sokolova-Lapa et al. 2021) only at low accretion rates. A tentative cyclotron resonant scattering feature (or cyclotron line) detection was reported by Tsygankov et al. (2012) at 32 keV which, however, has not been confirmed in other works. RX J0440's pulse profile is characterized by a single-peak, sine-like shape, plus a narrow dip observed in the soft X-ray band (Usui et al. 2012) attributed to absorption from the accretion stream (Galloway et al. 2001).

In this work, we report on the discovery of transient quasi-periodic oscillations (QPOs) observed by *Fermi*-GBM in RX J0440 during its latest outburst in 2023. The observed QPOs are triple transient as they appear only above the critical luminosity, only at certain pulse phases, and only for a few oscillations at time. We propose that the

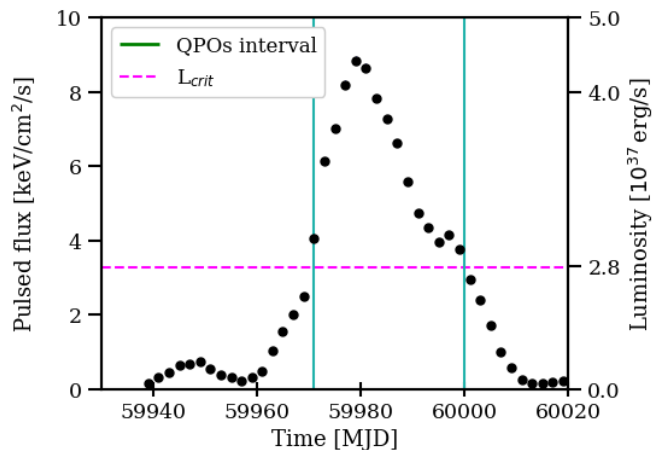


Fig. 1. GBM observations of RX J0440 during 2023 outburst. Black dots (with gray error bars) show the GBM (12–50 keV) three-day average pulsed flux. The horizontal magenta dashed line indicates the critical luminosity at 2.8×10^{37} erg/s (Salganik et al. 2023) as related to the right y-axis units. The nonlinearity in the right y-axis is due to a variable conversion factor at different outburst stages (see text). The light green vertical continuous lines mark the interval when the source is showing QPO episodes.

appearance of triple-transient quasi-periodic oscillations – or ATTO – is linked to the beaming pattern in the supercritical accretion regime coupled with the system geometry.

2. Observations and data reduction

Fermi-GBM (GBM hereafter) is the lower energy instrument aboard the *Fermi* Gamma-ray Space Telescope. It is an all-sky monitor instrument consisting of twelve sodium iodide (NaI) detectors and two bismuth germanate (BGO) detectors (Meegan et al. 2009). GBM’s configuration allows wide-field (>8 sr) broadband (8 keV - 40 MeV) observations of transient and persistent X-ray and γ -ray sources. Although designed to hunt for gamma-ray bursts, thanks to its continuous timing and spectral characterization of transient sources GBM has proved excellent in studying accreting XRPs as well through the GBM accreting pulsars program (GAPP, see Malacaria et al. 2020).

Fermi-GBM triggered on RX J0440 several times during the brightest part of the outburst, from January 26 to February 25, 2023 (MJD 59970 – 60000). Fig. 1 shows RX J0440 as observed by the GAPP during the outburst¹. The luminosity scale shown in Fig. 1 is obtained by converting the GBM pulsed flux to the *NuSTAR* luminosity values derived by Salganik et al. (2023), with a conversion factor that depends on the outburst stage. For the data analysis in this work, we considered time-tagged event (TTE – 128 energy channels, 2 μ s time binning) data from RX J0440 for events that triggered GBM on board. All GBM triggers from RX J0440 occur at the peak of the sine-like pulse profile, and show one or more flares. For each trigger we only analyze data from the three NaI detectors where the angle to the source is less than 60 deg. Moreover, for our analysis we only considered triggers showing three or more flares (see Fig. 2). A log of the analyzed triggers is shown in

¹ <https://gammaray.nsstc.nasa.gov/gbm/science/pulsars/lightcurves/rxj0440.html>

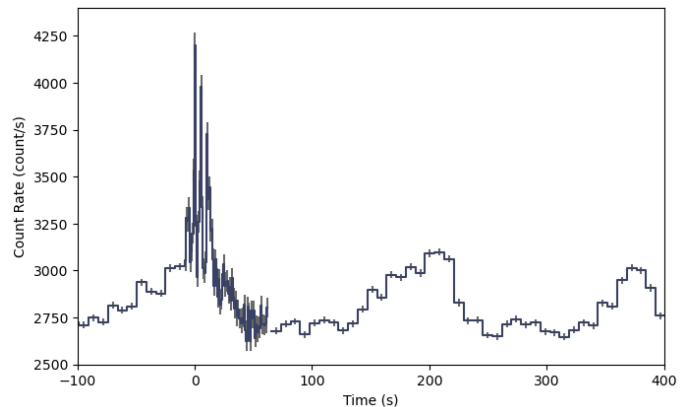


Fig. 2. GBM light curve of RX J0440 around trigger 230204.473 obtained by merging events from the NaI detectors N6, N7, and N8 in the 8–70 keV energy band and with a 1 s binning around the trigger (8 s otherwise). The sine-like long-term trend shows the source pulsation with an ~ 205 s periodicity. QPOs are evident at the peak of first pulse profile, around the GBM trigger time T_0 .

Table 1. Log of *Fermi*-GBM observations used in this work.

Trigcat	Date (MJD)
230203.275	59978.27
230204.473	59979.47
230206.376	59981.38
230206.723	59981.72
230206.797	59981.79
230209.271	59984.27
230211.733	59986.73
230218.657	59993.66

Table 1. For data filtering and analysis we used the GBM Data Tools² software, v1.1.1 (Goldstein et al. 2022).

3. Data analysis and results

We stacked TTE data for each trigger in Table 1 and relevant detectors to accumulate statistics (the GBM trigger catalog is published online³). Then, we limited the time window around the trigger time to one spin period (205 s) and used only data in the 8 – 70 keV energy band, above which the background dominates the signal. We used the combined event lists to construct light curves with a time resolution of $\Delta t = 0.00390625$ s, corresponding to a Nyquist frequency of $\nu_{Ny} = 128$ Hz. We produced a periodogram over the whole pulse period using the fractional rms normalization (Belloni & Hasinger 1990; Miyamoto et al. 1992) for each light curve using the software package *stingray* (Huppenkothen et al. 2019a; Huppenkothen et al. 2019b) and averaged all considered periodograms to improve statistics. The resulting averaged periodogram is shown in Fig. 3.

The typical periodogram observed in accreting XRP is mainly composed of aperiodical variability (noise) in the form of a low-frequency power-law with a break due to the magnetospheric boundary (Lyubarskii 1997). Above

² https://fermi.gsfc.nasa.gov/ssc/data/analysis/rmfit/gbm_data_tools/gdt-docs/.

³ <https://heasarc.gsfc.nasa.gov/W3Browse/fermi/fermigtrig.html>

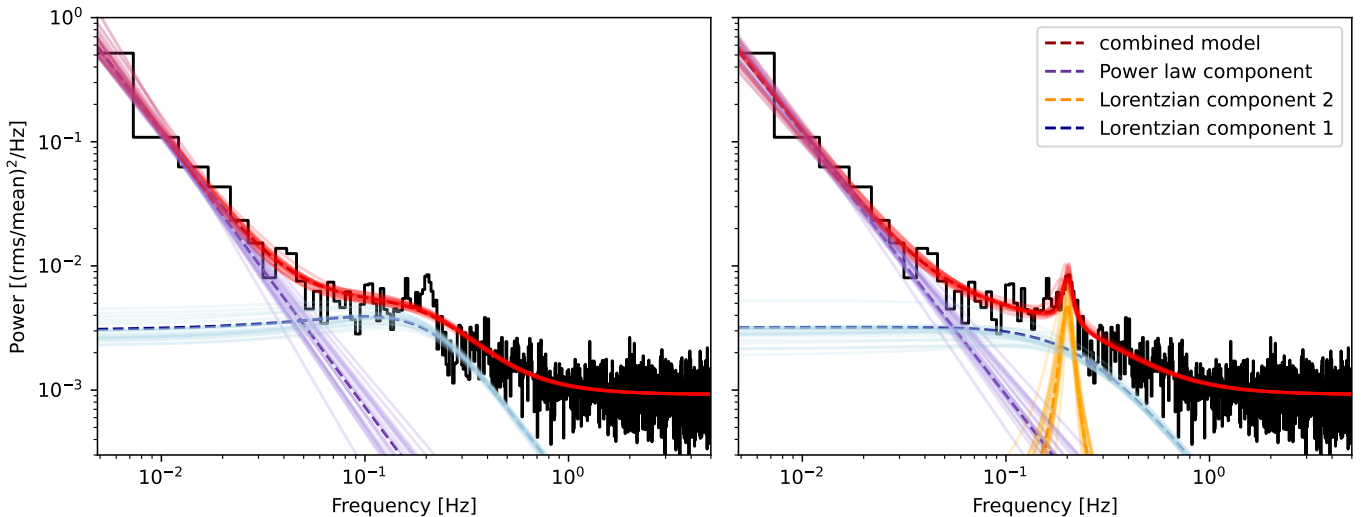


Fig. 3. Averaged periodogram of RX J0440 data. In red, we show the combined model for \mathcal{M}_1 (left) and \mathcal{M}_2 (right), in purple, we show the power-law components, and in blue and orange we show the two Lorentzians (only one for \mathcal{M}_1) – each of which includes a constant white noise component. Dashed lines represent the median of the posterior predictive distribution, and lightly shaded solid lines correspond to twenty individual draws from the posterior predictive distribution, for each of the model components as well as the combined model.

the break the power law slope becomes steeper, which is suggestive of a smoother magnetospheric flow (Revnivtsev et al. 2009), typically modeled with a Lorentzian component (Mönkkönen et al. 2022). The average periodogram from RX J0440 shows a strong noise component at low frequencies, as well as additional excess power in the 0.1-1 Hz band. In order to assess the significance of the excess power, we fit a model combining a power law for the low-frequency noise component with one Lorentzian for the excess noise (model 1, denoted \mathcal{M}_1) or a combination of a power law with two Lorentzian components (model 2, \mathcal{M}_2). We denote the Lorentzian components L_1 and L_2 , respectively. In both models, we also include a constant c to parameterize the flat noise component at high frequencies (white noise). We parameterized the power law in terms of an amplitude, A_{PL} and power law index α , the Lorentzian with the amplitude A_{Lor} , the centroid frequency, ν_{mid} and the quality factor $Q = \nu_{mid}/\gamma$, where γ is the full width at half maximum.

We estimated the Bayes factor $\log(\mathcal{B}_{12})$ to compare the two models and we find $\log(\mathcal{B}_{12}) = -30.3$, indicating decisive evidence for \mathcal{M}_2 (and the presence of a QPO-like component in the periodogram) following the scale of Kass & Raftery (1995) for the interpretation of the Bayes factor. For L_2 , we find a centroid frequency of $\nu_{mid,2} = 0.199^{+0.003}_{-0.004}$, a quality factor $Q_2 = 16.4^{+7.4}_{-5.1}$, and an amplitude $A_{Lor,2} = 0.005^{+0.002}_{-0.001}$, where we report the median of the posterior distribution and the 1σ credible intervals. We report supplementary statistical details of the analysis in Appendix A. Moreover, given that the strongest variability appears at the peak of the source pulse profile (see Fig. 2), we also obtain periodograms corresponding to different phases of the spin period to test for spin-phase dependence. To obtain phase-resolved periodograms, we defined six (overlapping) segments lasting 75 s each and covering different phases of the pulse profile, starting 25 s apart (see Fig. 4). We marked the phase corresponding to the pulse profile peak as 0.5. For

each segment, we modeled the averaged periodogram across all included cycles with the two above-mentioned models, \mathcal{M}_1 and \mathcal{M}_2 . We find that segments that do not include the time around a phase of ~ 0.5 generally favor model \mathcal{M}_1 , while segments covering the peak of the pulse profile very strongly prefer model \mathcal{M}_2 and the presence of a narrow, QPO-like feature, suggesting that the QPO is transient and phase-dependent (see Fig. 4 and Appendix A for more details). Finally, we notice that the limited statistics of the intrinsically transient phenomenon prevents a luminosity-independent analysis of the QPOs.

Finally, to explore possible spectral variations of the X-ray emission during the observed QPOs episodes, we defined a hardness ratio as the ratio between the photon counts in two energy bands, that is, $HR = 20-70 \text{ keV} / 8-20 \text{ keV}$. The energy intervals were chosen to ensure comparable statistics in both bands. We analyzed the HR around the triggers down to a time binning of 0.5 s. We find that the HR does not show significant variation within the TTE files' durations, sampling a few spin cycles each.

4. Discussion

4.1. QPOs from the Keplerian frequency model

We discovered the appearance of triple-transient QPOs (ATTO) in RX J0440 at a frequency of ~ 0.2 Hz. QPOs in the range from mHz to ~ 10 Hz have been observed in several XRPs (Reig 2008; James et al. 2010; Sidoli et al. 2016; Nespoli & Reig 2011; Wilson-Hodge et al. 2018). In some systems, QPOs are persistent, while more often they are transient. Widely accepted QPO models feature an accretion disk whose inner radius is directly interacting with the NS magnetosphere. For those models, QPOs are either the result of an accreting inhomogeneity rotating at the magnetospheric radius with the disk Keplerian frequency $\nu_{QPO} = \nu_K(r_m)$ (Keplerian frequency model, or KM, van der Klis 1989), or due to variations in the accre-

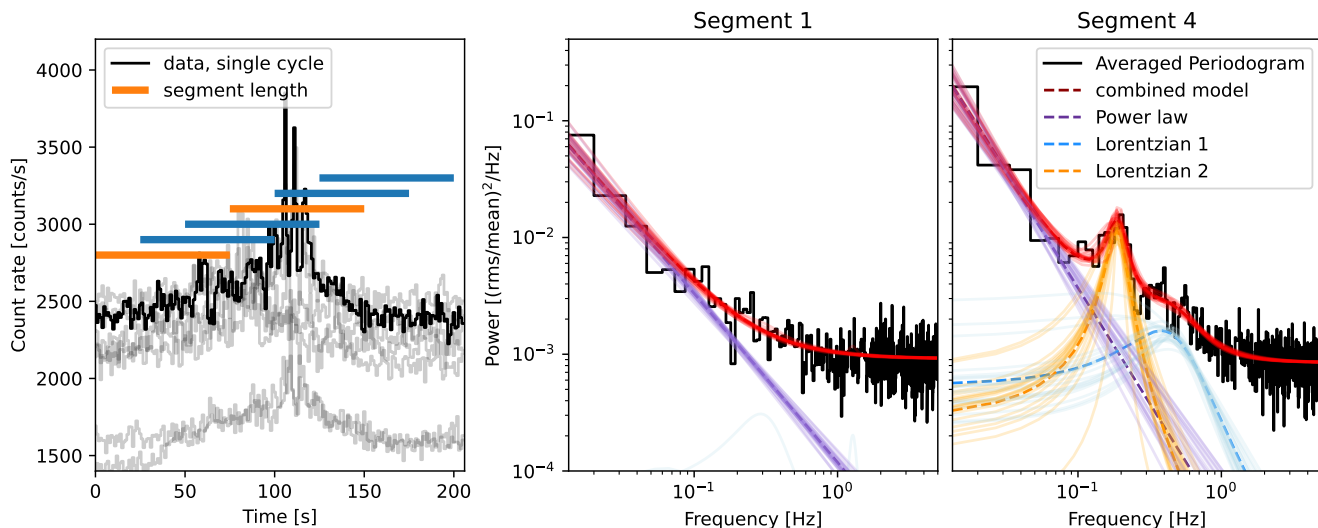


Fig. 4. Phase-resolved results for RX J0440. *Left:* Aligned light curves (in gray) of the triggers in Table 1 – one highlighted in black for clarity. Horizontal bars correspond to the segments used for the phase-resolved analysis. Orange bars represent segments in phase used to produce the right panels. *Right:* Periodograms of RX J0440 data at different spin phases, corresponding to segments 1 and 4, as indicated on top. Symbols are as in Fig. 3. The segment 1 panel shows the periodogram resulting from data outside of the pulse profile peak, when the periodogram does not require a second Lorentzian component. The segment 4 panel shows the periodogram obtained from pulse-profile peak-centered data, where a second Lorentzian component is required at ~ 0.2 Hz.

tion rate at a characteristic frequency equal to the beat frequency between the accretion disk and the NS spin frequency, $\nu_{QPO} = \nu_{beat} = \nu_K(r_m) - \nu_{spin}$, which is the beat frequency model (BFM, Alpar & Shaham 1985; Lamb et al. 1985). The Keplerian frequency at the inner disk radius r_K is equal to

$$\nu_K = \sqrt{\frac{GM_{NS}}{(2\pi)^2 r_K^3}}, \quad (1)$$

where M_{NS} is the NS mass. From Eq. 1, the inner disk radius is $r_K = (GM/(2\pi\nu_K)^2)^{1/3}$. On the other hand, the magnetospheric radius is $r_m = k r_A$, where r_A is the Alfvén radius when the energy density of the magnetic field balances the kinetic energy density of the infalling material (Davies & Pringle 1981):

$$r_A = \left(\frac{\mu^4}{2GM_{NS}\dot{M}^2} \right)^{1/7}, \quad (2)$$

while k is the coupling constant and $\mu = \frac{1}{2}BR_{NS}^3$ is the magnetic dipole moment (with magnetic field strength B and NS radius R_{NS}). Since $\nu_{QPO} \gg \nu_{spin}$, ν_{QPO} in the BFM is still $\sim \nu_K$. Therefore, assuming the KM, we can write $r_m = r_K$, from which we find

$$\mu = 1.9 \times 10^{31} \text{ G cm}^3 k_{0.5}^{-7/4} M_{1.4}^{5/6} \dot{M}_{-8}^{1/2} \left(\frac{\nu_k}{0.2 \text{ Hz}} \right)^{-7/6} \quad (3)$$

where $M_{1.4}$ is the NS mass in units of $1.4 M_\odot$, $k_{0.5}$ is the coupling constant in units of 0.5, and \dot{M}_{-8} is the mass accretion rate in units of $10^{-8} M_\odot \text{ yr}^{-1}$. Salganik et al. (2023) finds a luminosity of $\sim 3 \times 10^{37} \text{ erg/s}$ which, for an efficiency of $\eta = 0.17$, corresponds to a mass accretion rate of $3.1 \times 10^{-9} M_\odot \text{ yr}^{-1}$. Assuming $k = 0.5$, and given that for the Keplerian model $\nu_{QPO} \gg \nu_{spin}$ implies $\nu_K = \nu_{QPO}$, then Eq. 3 returns a magnetic field of $2.3 \times 10^{13} \text{ G}$ (however, see Bozzo et al. 2009, 2018 for a discussion about the underlying assumptions in this approach). Salganik et al. (2023)

excluded the presence of a cyclotron line in recent observations of RX J0440 and used other arguments to estimate a magnetic field of $\sim 10^{13} \text{ G}$, in line with our findings.

4.2. Comparison with EXO 2030+375 and other XRPs

The QPOs frequency in RX J0440, $\sim 0.2 \text{ Hz}$, is remarkably similar to that found in another XRP, EXO 2030+375 (Angelini et al. 1989). Moreover, the newly discovered QPOs share additional similarities with the QPOs observed in other XRPs. First, similarly to EXO 2030+375 and several other accreting XRPs, the Q factor of the QPOs in RX J0440 is relatively low when compared to the Q factor of the QPOs observed in other accreting systems (Reig 2008). Furthermore, the QPOs discovered in EXO 2030+375 were also transient and detected only around the peak of a bright outburst, at a 1–20 keV luminosity larger than $1.8 \times 10^{37} \text{ erg/s}$ (corrected from the luminosity reported in Angelini et al. 1989 for a Gaia DR3 distance of 2.4 kpc). Likewise, GBM detections of the QPOs in RX J0440 start on MJD 59970 at a (1–79 keV) luminosity of about $2.8 \times 10^{37} \text{ erg s}^{-1}$ (Salganik et al. 2023), while QPOs are no longer detected after MJD 60000, which is when the source luminosity drops below the same value (see also Appendix B for the non-detection significance). Although not explicitly reported in previous works, we notice that such behavior is similar to that observed in other XRPs, where QPOs are not detected in the subcritical regime corresponding to the horizontal branch in the hardness-intensity diagram (Reig 2008). Similar findings are also obtained for the XRP 1A 0535+262 (Finger et al. 1996), where QPOs are observed when the source luminosity is above $6 \times 10^{36} \text{ erg/s}$ (assuming a Gaia DR3 distance of 1.8 kpc), in agreement with the critical luminosity value derived by Mushtukov et al. (2015, see their Fig. 7), but not when the source luminosity drops below the same value. However, the opposite is also observed for sources for which QPOs are detected only

in the subcritical regime (see, e.g., KS 1947+300, James et al. 2010).

It is therefore tempting to associate the appearance of QPOs in RX J0440 with the onset of the supercritical accretion regime. Accordingly, we speculate upon the following qualitative scenario. When the source enters the supercritical accretion regime forming an accretion column at the magnetic poles, the radiation beaming pattern changes from a pencil-beam to a fan-beam pattern (Basko & Sunyaev 1976; Becker et al. 2012). Depending on the system geometry, radiation in this regime can be more likely to hit the inner accretion disk (see, e.g., Koliopanos & Vasilopoulos 2018). The geometry recently proposed for RX J0440 (Doroshenko et al. 2023) with a magnetic obliquity of $\sim 48^\circ$ is consistent with this condition (assuming that the accretion disk is perpendicular to the spin axis). When the radiation hits the disk, if the inner accretion disk viscosity is stochastically unstable in relation to the mass accretion rate and temperature variations (see, e.g., Romanova et al. 2008, Potter & Balbus 2014), “tongues” of enhanced accretion can form at the disk inner radius r_K and subsequently accrete onto the magnetic poles, thus feeding the observed QPOs. However, we note that simulations by Romanova et al. 2008 consider an NS with a relatively low magnetic field typical of millisecond X-ray pulsars. It remains to be demonstrated if a phenomenology similar to the tongues revealed by those simulations can also appear in the case of highly magnetized neutron stars. Besides, QPOs in RX J0440 are only observed at the peak of the pulse profile. This observational aspect is likely related to the system geometry. To this aim, we notice that the sharp dip observed in the RX J0440 pulse profile was interpreted as emission eclipsed by the accretion stream (Usui et al. 2012; Galloway et al. 2001). This supports the idea that, in RX J0440, the pulse profile peak represents the emission from the accretion column observed at the closest approach to the observer line of sight. Under such circumstances, if the QPOs’ emission originates at the bottom of the accretion column, when the column becomes occulted by the NS rotation then the QPOs also become invisible to the observer, thus appearing as spin-phase-dependent QPOs. Finally, beaming or collimation of the original X-ray emission by the surrounding matter and expelled winds might also influence the appearance of QPOs, although only in pulsating Ultra Luminous X-ray sources are such effects expected to result in highly beamed escaping radiation (Abarca et al. 2021; King et al. 2023).

Acknowledgements. This work has made use of data from the European Space Agency (ESA) mission *Gaia* (<https://www.cosmos.esa.int/gaia>), processed by the *Gaia* Data Processing and Analysis Consortium (DPAC, <https://www.cosmos.esa.int/web/gaia/dpac/consortium>). O.J.R. gratefully acknowledges NASA funding through contract 80MSFC17M0022.

References

- Abarca, D., Parfrey, K., & Kluźniak, W. 2021, *ApJ*, 917, L31
 Alpar, M. A., & Shaham, J. 1985, *Nature*, 316, 239
 Angelini, L., Stella, L., & Parmar, A. N. 1989, *ApJ*, 346, 906
 Barret, D., & Vaughan, S. 2012, *ApJ*, 746, 131
 Basko, M. M., & Sunyaev, R. A. 1976, *MNRAS*, 175, 395
 Becker, P. A., Klochkov, D., Schönherr, G., et al. 2012, *A&A*, 544, A123
 Belloni, T., & Hasinger, G. 1990, *A&A*, 227, L33
 Bozzo, E., Ascenzi, S., Ducci, L., et al. 2018, *A&A*, 617, A126
 Bozzo, E., Stella, L., Vietri, M., & Ghosh, P. 2009, *A&A*, 493, 809
 Bradbury, J., Frostig, R., Hawkins, P., et al. 2018, JAX: composable transformations of Python+NumPy programs
 Chatfield, C. 2013, *The analysis of time series: theory and practice* (Springer)
 Coley, J., Gendreau, K., Pottschmidt, K., et al. 2023, *ATel*, 15907, 1
 Davies, R. E., & Pringle, J. E. 1981, *MNRAS*, 196, 209
 Dickey, J. M., & Lientz, B. P. 1970, *The Annals of Mathematical Statistics*, 41, 214
 Doroshenko, V., Poutanen, J., Heyl, J., et al. 2023, *A&A*, 677, A57
 Finger, M. H., Wilson, R. B., & Harmon, B. A. 1996, *ApJ*, 459, 288
 Fitzpatrick, G., Connaughton, V., McBreen, S., & Tierney, D. 2011, arXiv e-prints, arXiv:1111.3779
 Gaia Collaboration, Vallenari, A., Brown, A. G. A., et al. 2022, arXiv e-prints, arXiv:2208.00211
 Galloway, D. K., Giles, A. B., Wu, K., & Greenhill, J. G. 2001, *MNRAS*, 325, 419
 Goldstein, A., Cleveland, W. H., & Kocevski, D. 2022, *Fermi GBM Data Tools: v1.1.1*
 Homan, M. D., & Gelman, A. 2014, *J. Mach. Learn. Res.*, 15, 1593–1623
 Huebner, M., Huppenkothen, D., Lasky, P. D., & Inglis, A. R. 2021, arXiv e-prints, arXiv:2108.07418
 Huppenkothen, D., Bachetti, M., Stevens, A. L., et al. 2019a, *ApJ*, 881, 39
 Huppenkothen, D., Bachetti, M., Stevens, A. L., et al. 2019b, *Journal of Open Source Software*, 4, 1393
 James, M., Paul, B., Devasia, J., & Indulekha, K. 2010, *MNRAS*, 407, 285
 Kass, R. E., & Raftery, A. E. 1995, *Journal of the American Statistical Association*, 90, 773
 King, A., Lasota, J.-P., & Middleton, M. 2023, *New A Rev.*, 96, 101672
 Koliopanos, F., & Vasilopoulos, G. 2018, *A&A*, 614, A23
 Lamb, F. K., Shibazaki, N., Alpar, M. A., & Shaham, J. 1985, *Nature*, 317, 681
 Lao, J., & Louf, R. 2020, *Blackjax: A sampling library for JAX*
 Lao, J., Suter, C., Langmore, I., et al. 2020, arXiv e-prints, arXiv:2002.01184
 Lyubarskii, Y. E. 1997, *MNRAS*, 292, 679
 Malacaria, C., Jenke, P., Roberts, O. J., et al. 2020, *ApJ*, 896, 90
 Mandal, M., Pal, S., Gendreau, K., et al. 2023, *ATel*, 15848, 1
 Meegan, C., Lichti, G., Bhat, P. N., et al. 2009, *ApJ*, 702, 791
 Miyamoto, S., Kitamoto, S., Iga, S., Negoro, H., & Terada, K. 1992, *ApJ*, 391, L21
 Mönkkönen, J., Tsygankov, S. S., Mushtukov, A. A., et al. 2022, *MNRAS*, 515, 571
 Motch, C., Haberl, F., Dennerl, K., Pakull, M., & Janot-Pacheco, E. 1997, *A&A*, 323, 853
 Mushtukov, A. A., Suleimanov, V. F., Tsygankov, S. S., & Portegies Zwart, S. 2021, *MNRAS*, 503, 5193
 Mushtukov, A. A., Suleimanov, V. F., Tsygankov, S. S., & Poutanen, J. 2015, *MNRAS*, 447, 1847
 Nakajima, M., Negoro, H., Mihara, T., et al. 2022, *ATel*, 15835, 1
 Nespoli, E., & Reig, P. 2011, *A&A*, 526, A7
 Pal, S., Mandal, M., Gendreau, K., et al. 2023, *ATel*, 15868, 1
 Phan, D., Pradhan, N., & Jankowiak, M. 2019, arXiv e-prints, arXiv:1912.11554
 Potter, W. J., & Balbus, S. A. 2014, *MNRAS*, 441, 681
 Reig, P. 2008, *A&A*, 489, 725
 Reig, P., Negueruela, I., Fabregat, J., Chato, R., & Coe, M. J. 2005, *A&A*, 440, 1079
 Reig, P., & Roche, P. 1999, *MNRAS*, 306, 100
 Revnivtsev, M., Churazov, E., Postnov, K., & Tsygankov, S. 2009, *A&A*, 507, 1211
 Romanova, M. M., Kulkarni, A. K., & Lovelace, R. V. E. 2008, *ApJ*, 673, L171
 Salganik, A., Tsygankov, S. S., Doroshenko, V., et al. 2023, *MNRAS*, 524, 5213
 Sidoli, L., Esposito, P., Motta, S. E., Israel, G. L., & Rodríguez Castillo, G. A. 2016, *MNRAS*, 460, 3637
 Sokolova-Lapa, E., Gornostaev, M., Wilms, J., et al. 2021, *A&A*, 651, A12
 Tsygankov, S. S., Doroshenko, V., Mushtukov, A. A., et al. 2019, *MNRAS*, 487, L30
 Tsygankov, S. S., Krivonos, R. A., & Lutovinov, A. A. 2012, *MNRAS*, 421, 2407
 Usui, R., Morii, M., Kawai, N., et al. 2012, *PASJ*, 64, 79
 van der Klis, M. 1989, in *NATO Advanced Science Institutes (ASI) Series C*, ed. H. Ögelman & E. P. J. van den Heuvel, Vol. 262, 27
 Vaughan, S., Edelson, R., Warwick, R. S., & Uttley, P. 2003, *MNRAS*, 345, 1271
 Whittle, P. 1951, *Hypothesis testing in time series analysis*, Vol. 4 (Almqvist & Wiksells boktr.)
 Wilson-Hodge, C. A., Malacaria, C., Jenke, P. A., et al. 2018, *ApJ*, 863, 9

Appendix A: Supplementary statistical material

We define a Whittle likelihood (Whittle 1951; Chatfield 2013) appropriate for averaged periodograms as introduced in Barret & Vaughan (2012). We applied wide, uninformative priors as listed in Table A.1. We parameterized all parameters that can vary over more than an order of magnitude or that require us to enforce positivity in terms of the logarithm of the parameter. Despite the requirement that the amplitude be positive, we note that \mathcal{M}_1 is a special case of \mathcal{M}_2 if the amplitude of the Lorentzian in the second component is zero. This allows for a relatively straightforward model comparison, and thus we designed \mathcal{M}_2 with that model comparison in mind, and a uniform prior on the amplitude itself rather than the logarithm.

We constructed the model using the JAX *python* library (Bradbury et al. 2018). We sampled the posterior using the Hamiltonian Monte Carlo method, which uses first-order gradient information for efficient exploration of the parameter space, with the No U-Turn Sampler (NUTS; Homan & Gelman 2014; Phan et al. 2019; Lao et al. 2020) extension as implemented in the Python package *blackjax* (Lao & Louf 2020). In Figure 3, we present the comparison between the two models. The second component models a narrow feature at ~ 0.2 Hz. We note that the posterior distribution for the amplitude, $A_{\text{Lor},2} = 0.005^{+0.002}_{-0.001}$, assigns no probability to $A_{\text{Lor},2} = 0$, which corresponds to the simpler model \mathcal{M}_1 .

We used the nested nature of our models and employed the Savage-Dickey density ratio (SDDR; Dickey & Lientz 1970) to estimate the Bayes factor to compare the two models. The Bayes factor can be estimated from the marginal posterior density for $p(A_{\text{Lor},2}|D)$ and the prior $p(A_{\text{Lor},2})$. We find a Bayes factor of $\log(\mathcal{B}_{12}) = -30.3$, which strongly favors the \mathcal{M}_2 (assuming equal prior probabilities for \mathcal{M}_1 and \mathcal{M}_2).

There are two notable caveats to this result. Firstly, Bayes factors generally depend strongly on prior assumptions. A sensitivity analysis of the result on the prior for the amplitude of L_2 reveals that even dramatically increasing the prior volume by two orders of magnitude only lowers the Bayes factor to $\log(\mathcal{B}_{12}) = -23.4$, which, while lower, would still be interpreted as decisive evidence for \mathcal{M}_2 . The second caveat concerns the use of periodograms for this analysis; the data considered here breaks some of the assumptions made during the statistical analysis of periodograms, most notably stationarity and a purely stochastic process. Huebner et al. (2021) showed that the presence of non-stationarity in light curves breaks independence assumptions made in the definition of the likelihood, and as a consequence signals may appear more significant than they are in reality. However, we note that the detection here is highly significant (a Bayes factor of $\log(\mathcal{B}_{12}) = -30$ corresponds to odds of $\sim 10^{14} : 1$), and we expect it to remain highly significant even when accounting for the non-stationarity.

Similarly, for the phase-resolved analysis we calculated the Bayes factor \mathcal{B}_{12} using the SDDR for each segment and model choice. We find (see Fig. 4) that segments not including the time around the phase ~ 0.5 (segments 1, 2, and 6) return Bayes factors favoring model \mathcal{M}_1 ($\log(\mathcal{B}_{12}) = 3.5, 0.5, 1.4$, respectively), while segments covering the peak of the pulse profile (segments 3, 4, and 5) have Bayes factors that very strongly prefer model \mathcal{M}_2 and the presence of a narrow, QPO-like feature at ~ 0.2 Hz ($\log(\mathcal{B}_{12}) = -23.9, -50.7, -42.3$, respectively).

Table A.1. Priors applied to the two models, \mathcal{M}_1 and \mathcal{M}_2 .

Component	Parameter	Distribution
Power law	$\log(A_{\text{PL}})$	$\mathcal{N}(-10, 5)^b$
	α	$\mathcal{N}(3, 2)$
Lorentzian 1	$\log(A_{\text{Lor},1})$	$\mathcal{N}(-5, 5)$
	$\log(\nu_{\text{mid},1})$	$\mathcal{U}(\log(0.0049), \log(10))^c$
	$\log(Q_1)$	$\mathcal{U}(\log(0.01), \log(2))$
Lorentzian 2 ^a	$A_{\text{Lor},2}$	$\mathcal{U}(0, 1.0)$
	$\log(\nu_{\text{mid},2})$	$\mathcal{U}(\log(0.0049), \log(10))$
	$\log(Q_2)$	$\mathcal{U}(\log(2), \log(50))$
Counting noise	$\log(C)$	$\mathcal{N}(\log(\mu_n), \log(\mu_n/5))^d$

Notes. ^(a) This component is only present in \mathcal{M}_2 . ^(b) $\mathcal{N}(\mu, \sigma^2)$ defines a normal distribution with a mean of μ and a variance of σ^2 . ^(c) $\mathcal{U}(a, b)$ defines a uniform distribution with lower bound a and upper bound b . ^(d) For simplicity, and because the noise in GBM is generally well-behaved, the prior for the white noise component is set using the mean power μ_n of the last 100 frequencies in the periodogram.

We also notice that individual segments in the phase-resolved analysis necessarily include trends over the duration of the segments, as each segment captures a subset of the overall rise and fall of the pulse period. Trends on timescales longer than the length of a time series will redistribute power from below the smallest observable frequency into the observable frequency band, an effect called red noise leakage (see, e.g., Vaughan et al. 2003 for a discussion in the context of astronomical X-ray light curves). However, this largely affects the broadband noise properties, that is, the power-law index of the broadband power-law components in our model, not a QPO. The leakage might have a small, subtle effect on QPO detectability owing to the mildly distorted shape of the broadband periodogram against which we detected the QPOs. This effect could be calibrated with extensive simulations. However, we note that the broadband noise components in segments 1, 2, and 6, which largely exclude the phase segments with strong variability, are relatively flat, with a power-law index $\alpha \approx 1.5$. Vaughan et al. (2003) suggested that red noise leakage is negligible for similar spectra, so we expect the effect to be minor compared to the dramatic differences in Bayes factor we find for the different segments.

Appendix B: Significance of ATTO non-detection

To demonstrate that the non-detection of QPOs in RX J0440 below the critical luminosity is not due to GBM sensitivity but that it is a physical effect, we compare the GBM background variability with the GBM triggering criteria. To this aim, we sampled TTE hourly data from Jan. 22, 2023 (MJD 59966.759), which is four days before the first GBM trigger from RX J0440 (MJD 59970.759) and corresponds to an $\sim 50\%$ lower GBM pulsed flux from this source. This date was chosen because the *Fermi* spacecraft is approximately in the same orbital location and orientation approximately every ~ 48 hours (Fitzpatrick et al. 2011); thus the instrument sensitivity is comparable approximately every two days. At the same time, the sampled date corresponds to the subcritical accretion regime (Salganik et al. 2023). We verified that source pulsations were observed in the TTE data around MJD 59966.759, although

the source did not trigger the instrument. A GBM trigger occurs when the instrument detects a signal with a significance of $> 4.5\sigma$ in at least two NaI detectors. The typical significance (S/N) of the QPO flares from triggers in Table 1 is $> 10\sigma$ for the detectors with the smallest source angles. Given the highly variable background in GBM (up to a factor of ~ 2 over one orbit), we estimate that a QPO flare event similar to those detected on MJD 59970.759 (with $\text{SNR} \sim 10\sigma$) would have triggered GBM on MJD 59966 for all possible background rates registered by the detectors with the smallest source angles. This implies that, although we cannot exclude ATTO occurring at times where GBM had no coverage or had less sensitivity due to particularly noisy events (such as solar flares or incident particles), the strength of the QPO signal, if ever present, has weakened significantly at subcritical luminosity.